Journal of Alloys and Compounds 1056 (2026) 186611

Contents lists available at ScienceDirect

Journal of Alloys and Compounds

journal homepage: www.elsevier.com/locate/jalcom

Impact of B_4C ceramic doping on the mechanical and electrochemical properties of AlCoCrFeNi equimolar HEA

Alberto Daniel Rico-Cano [a,b,*], Göknur Karadeniz [b], Gultekin Goller [b], Julia Claudia Mirza-Rosca [a,c]

[a] Universidad de Las Palmas de Gran canaria, Dpto. de Ingeniería Mecánica, Campus Universitario Tafira, Las Palmas de gran Canaria 35017, Spain
[b] Istanbul Technical University, Department of Metallurgical and Materials Engineering, Maslak, Istanbul 34469, Turkey
[c] Transilvania University of Brasov, Materials Engineering and Welding Department, Brasov 500036, Romania

ARTICLE INFO

Keywords:
High-entropy alloys
Boron carbide
Spark plasma sintering
Microstructure
Corrosion
Hardness
Segregation

ABSTRACT

This work examines the influence of adding 2 % boron carbide (B_4C) to an AlCoCrFeNi high-entropy alloy processed by spark plasma sintering under identical conditions. The study combines microstructural characterization, electrochemical evaluation and statistical microhardness analysis to determine how the ceramic addition modifies the behavior of the alloy. Scanning electron microscopy and optical metallography revealed that the undoped alloy presents a relatively uniform matrix with limited contrast variations. In contrast, the B_4C-reinforced sample shows a more heterogeneous structure, marked by a broader range of gray levels and a clearer separation of phases. Chromium-rich regions were identified in both materials, consistent with the high melting point of Cr and the solid-state nature of the mechanical alloying route. In the doped sample, boron and carbon tended to accumulate within these Cr-rich domains, following their mixing enthalpy preferences. Electrochemical testing in chloride solution indicated that the addition of B_4C reduces corrosion resistance, with the doped material exhibiting lower stability during open-circuit measurements and a decreased charge-transfer resistance in impedance spectra. Mechanical testing showed that the 2 % B_4C addition increases Vickers hardness, although the hardness distribution becomes less uniform, as reflected by a higher dispersion in the statistical parameters. Overall, the results indicate that B_4C reinforcement strengthens the alloy but introduces greater microstructural heterogeneity and compromises corrosion performance.

1. Introduction

In 2004, another way of understanding metallic systems was discovered, High Entropy Alloys (HEAs). These are outstanding metallic compounds develop at 5 five principal elements in same atomic proportions [1,2]. By their superior possible combination, many different properties could be enhanced, such as higher melting points, hardness, corrosion resistances or fracture toughness. Therefore, their application range increased, as their demand on biomaterial [3], tribology [4], energetic [5] or refractory [6–8] industrial fields. These new types of metallic alloys have shown outstanding mechanical and chemical stability, together with a notable adaptability that depends strongly on their elemental balance, processing route and possible reinforcements [9].

Recent works has shown that different HEA exhibits strong corrosion resistance in aggressive environments. This behavior is mainly related to chemically uniform and stable passive films on the material surface [10,11]. In parallel, the inherent lattice distortion of HEAs contributes to high resistance against wear. Low wear rates and stable friction responses have been reported under sliding and abrasive conditions [12].

Oxidation resistance is also a key property of HEA, especially for those intended for elevated temperature services or in extreme demanding environments. Different studies indicate that selected compositions can form dense and adherent oxide layers. These layers effectively limit oxygen transport and slow degradation kinetics, particularly in Cr and Mo containing HEA, due to their oxides stability [13].

Among the different systems reported, the AlCoCrFeNi alloy is one of the most widely investigated and its synthesis routes and resulting properties are well documented in the literature [14–16]. This alloy can

* Corresponding author at: Universidad de Las Palmas de Gran canaria, Dpto. de Ingeniería Mecánica, Campus Universitario Tafira, Las Palmas de gran Canaria 35017, Spain
E-mail address: alberto.rico101@alu.ulpgc.es (A.D. Rico-Cano).

https://doi.org/10.1016/j.jallcom.2026.186611
Received 15 December 2025; Received in revised form 27 January 2026; Accepted 2 February 2026
Available online 5 February 2026

be produced through multiple fabrication techniques and is often formulated with variable aluminum contents. Instead of keeping an equiatomic ratio, it is commonly denoted as $Al_xCoCrFeNi$, where x typically ranges from 0.2 to 1.5 [17–19]. The amount of Al controls the crystalline structure: for $x \leq 0.3$, the alloy exhibits a single FCC phase; when $0.3 < x \leq 0.6$, both BCC/B2 and FCC phases coexist; and for $x > 0.6$, the structure fully transitions to a BCC structure [20].

HEA-based composites are also frequently reported, either incorporating the HEA as a strengthening phase or reinforcing the alloy with additional materials [21,22]. Reinforcement approaches are highly varied, ranging from metallic additions to the integration of polymers or ceramics. Ceramic-based strengthening, particularly when combined with Spark Plasma Sintering (SPS), has led to substantial improvements in strength and wear resistance, expanding the engineering relevance of these systems. Common ceramic reinforcements include SiC [23,24], TiB_2 [25], TiC [26,27] or B_4C [28,29], all valued for their excellent mechanical stability. Between all ceramics B_4C ranks as the third hardest material known, which raises its interest as doping or matrix compound [30].

Boron carbide (B_4C) is distinguished by its low density, very high hardness, strong neutron absorption capacity, semiconductive behavior and elevated melting point, resulting in excellent thermal stability and strong corrosion resistance [31–33]. These attributes make it highly valuable for aggressive environment electronic devices, bulletproof armors, extremely high temperature refractory components and nuclear protection systems [34]. Its combination of light weight, mechanical strength and durability makes it a potential alternative to diamond for industrial use, being lighter and cheaper. B_4C-reinforced composites also show improved tribological performance compared to Si_3N_4, Al_2O_3, SiC or ZrO_2 ceramics, due to their high hardness and low density [35]. Therefore, B_4C ceramic presents a high interest in many technological and engineering fields, with uses ranging from nuclear engineering to structural and electronic applications [36].

This work examines the microstructural, mechanical and electrochemical behavior of two materials derived from an AlCoCrFeNi HEA matrix produced by SPS, one of which incorporates 2 % B_4C. By combining scanning electron microscopy with a series of electrochemical tests and a statistical Vickers microhardness test, the study evaluates how the addition of boron carbide modifies the corrosion response and general performance of this doped high-entropy alloy.

2. Experimental

2.1. Materials

The high-entropy alloy powders used in the study were mechanically alloyed at the Polytechnic University of Bucharest, Romania, using a Fritsch™ Pulverisette™ 6 Classic Line Planetary Mono Mill. The B_4C powder used as an additive was commercially supplied by H. C. Starck Cop. and the samples were sintered in the Spark Plasma Sintering (SPS-7.40 MK-VII, SPS Syntex Inc., Saitama, Japan) device located at Istanbul Technical University, Department of Metallurgy and Materials Engineering.

The sintering process was carried out under vacuum at 900°C under a constant uniaxial pressure of 40 MPa for 3 min. Information such as the production parameters and codes of the samples is provided in Table 1. The equimolar AlCoCrFeNi sample (named M1) and 2 % B_4C-doped AlCoCrFeNi (named M2) were obtained. For M2 system, powders were mixed for 6 h in a turbulent mixer (T2F Bachofen) to achieve complete homogenization before sintering. Graphite sheets are placed between punches and powders in the mold to facilitate conductivity during the SPS process.

The graphite paper adhering to the surface of the obtained samples was removed with SiC abrasive paper (120–2500 grit) in using the Struers TegraPol-11 system (Struers, Copenhagen, Denmark). The cleaned samples were polished using a 0.1 μm alpha alumina suspension for characterization processes.

2.1.1. Microstructural characterization

The microstructure characterization of the sintered samples was performed by three different methods. First, Scanning Electron Microscopy (SEM) test was performed using a Thermoscientific Axia ChemiSEM model scanning electron microscope. The analyses were performed at different magnifications of 500×, 2000× and 5000× to better understand the microstructure. Both EDS mapping and point EDS analyses were performed at 5000x magnification to observe the phase distributions in the microstructure. For a quantitative analysis of SEM images, software ImageJ has been used. This is an image analysis software extensively used by the microstructural characterization community for almost 20 years [37–39]. The second characterization step involved XRD analysis, in order to reveal the atomic structure and phase composition of the samples. This test was executed with the X'Pert PRO PANalytical X-ray Diffractometer, Cu-Kα radiation, 2θ: 10–110°. Finally, a metallographic examination using an optical microscope was performed. Before observation, the polished surfaces were electrochemically etched in a 10 % oxalic acid ($H_2C_2O_4$) solution, applying 5 V for 10 s to reveal the microstructural features. Surface images of the etched samples were then acquired with a Zeiss Axiocam ERc 5 s system (Carl-Zeiss QEC GmbH, Ostfildern, Germany).

2.1.2. Electrochemical tests

After preparing the samples, three electrochemical techniques: open circuit potential (OCP), linear polarization and electrochemical impedance spectroscopy (EIS), were performed using a BioLogic Essential SP-150 potentiostat in 3.5 % NaCl simulated seawater.

Test parameters and data analysis were carried out with EC-Lab v.9.55 software in compliance with ASTM G5–94 (2004) [40]. The cell employed a three-electrode configuration consisting of analyzed sample as the working electrode, a saturated calomel electrode as reference and a platinum mesh as counter electrode.

OCP was monitored for 24 h using the "E_{corr} vs. Time" method, with data logged every 30 s or upon a 100 mV potential shift, to assess passivation, stability or corrosion tendency. Linear polarization measurements were conducted after stabilization by defining the electrode surface area and duration (110 min). The potential was scanned from −0.1 to + 1 V vs. OCP at 10 mV/min and corrosion rates were calculated via Tafel fitting.

EIS, following ISO 16773–1–4:2016, was carried out by applying an AC signal over a frequency range of 100 mHz to 100 KHz [41]. The impedance response was represented using Nyquist and Bode plots, while equivalent circuit modeling was applied to simulate and interpret the electrochemical behavior of the material.

2.1.3. Vickers microhardness statistical analysis

Vickers microhardness tests were carried out with the use of FM-810 Microhardness Tester (Future Tech, Kawasaki, Japan), using a load of

Table 1
SPS production parameters of the samples.

Sample Codes	AlCoCrFeNi (vol%)	B_4C (vol%)	Sintering Temperature (°C)	Sintering Time (min)	Sintering Pressure (MPa)	Heating Rate (°C/min)
M1	100	-	900	3	40	100
M2	98	2	900	3	40	100

0.1 kgf ($HV_{0.1}$) and following ISO 14577–1:2015 standard [42]. This load was chosen to obtain reliable indentations while avoiding surface-roughness effects. For each sample, a total of 40 indentations were made to ensure good statistical significance. The hardness data were examined using three tools: boxplots to show quartiles and dispersion, histograms to display the distribution of values and fitted Gaussian curves to evaluate how close the results were to a normal distribution.

3. Results and discussion

3.1. Microstructural characterization

Fig. 1 shows magnifications of 500× and 2000× to the samples consolidated with SPS. Fig. 1, (a) shows dark gray phases within a homogeneous matrix in the microstructure of sample M1, its analysis on ImageJ determined that dark gray areas correspond to a 15 % of the surface fraction. For sample M2, as seen in (b), it is observed that the color contrast between the matrix and the dark-colored phases formed decreases with the addition of 2 % B_4C. Additionally, it is seen that these dark phase areas formed separately in the matrix are also wider. Its analysis on ImageJ confirmed that a bigger heterogeneity can be seen on the sample surface, classifying the gray tones and their surface fraction into 3; light gray (16.2 %), middle gray (62.6 %) and dark gray (21.2 %). The 2000× magnification is taken for more detailed examination, a generally homogeneous structure is seen in sample M1, while phase diversity is observed in sample M2. Additionally, it is seen that the pores have increased slightly with the B_4C addition.

The elemental distributions of the phases are shown in Fig. 2 and Fig. 3 for M1 and M2, respectively. Point EDS and mapping analysis were performed at 5000× magnification.

The results of the 5-point analysis performed on the different colored regions of the M1 sample in Fig. 2a) are given in Table 2. According to the table, chromium is particularly enriched in the dark regions. In the Cr-rich regions, the aluminum distribution is low, while the cobalt and nickel distributions are limited. In a similar study conducted by Li et al. [43], Cr-rich regions were also observed in the microstructure of samples produced by SPS. The authors stated that this situation occurred because chromium has a higher hardness than other elemental powders during mechanical alloying, causing it to remain in large particles and weld with other small elemental particles. They interpreted this as causing Cr to segregate. In the study conducted by Onawale et al. [44], it was stated that Cr is the element with the highest melting point (1907 °C) in the system and will be the first element to solidify during solidification. It was stated that in the equimolar system, Cr remains separate within the structure up to 1350 °C, while Al, with its low melting point (600 °C), has the highest diffusivity coefficient and stabilizes the BCC phase.

When examining the EDS mapping in Fig. 2, where each element is assigned a different color, images consistent with the above explanation are observed. The dark region is seen to be rich in chromium. Looking at aluminum, it can be interpreted that its distribution within the structure is lower compared to other elements.

Similar to M1, EDS point and mapping analyses were also performed for the M2 sample. The data from the point analyses are presented in Table 3. Points 1 and 2 show that the dark areas are chromium rich. An increase in boron and carbon values was observed along with the increase in Cr content, but aluminum and nickel content decreased. In Wu et al.'s study on CoCrFeNi alloy produced by adding B_4C using the laser powder bed fusion method, B and C were also observed in C-rich regions. This phenomenon was explained by the fact that the mixture enthalpy between Cr and C (-61 kJ/mol) had a higher absolute value than the mixture enthalpies of the other elements [Ni (-39 kJ/mol), Fe (-50 kJ/mol) and Co (-42 kJ/mol)] [45]. The area indicated by point 3 shows that Co-rich areas may also form within the structure, and their colors are lighter. The area at point 5 is seen to be rich in nickel and aluminum. In CoCrFeNiAl alloys, depending on the chemical composition, the chemical mixture enthalpy value in the Ni-Al binary phase system is −22 kJ/mol, which is the most negative value, thus enabling the formation of Ni-Al-rich phases [46]. Considering the area at point 6, boron

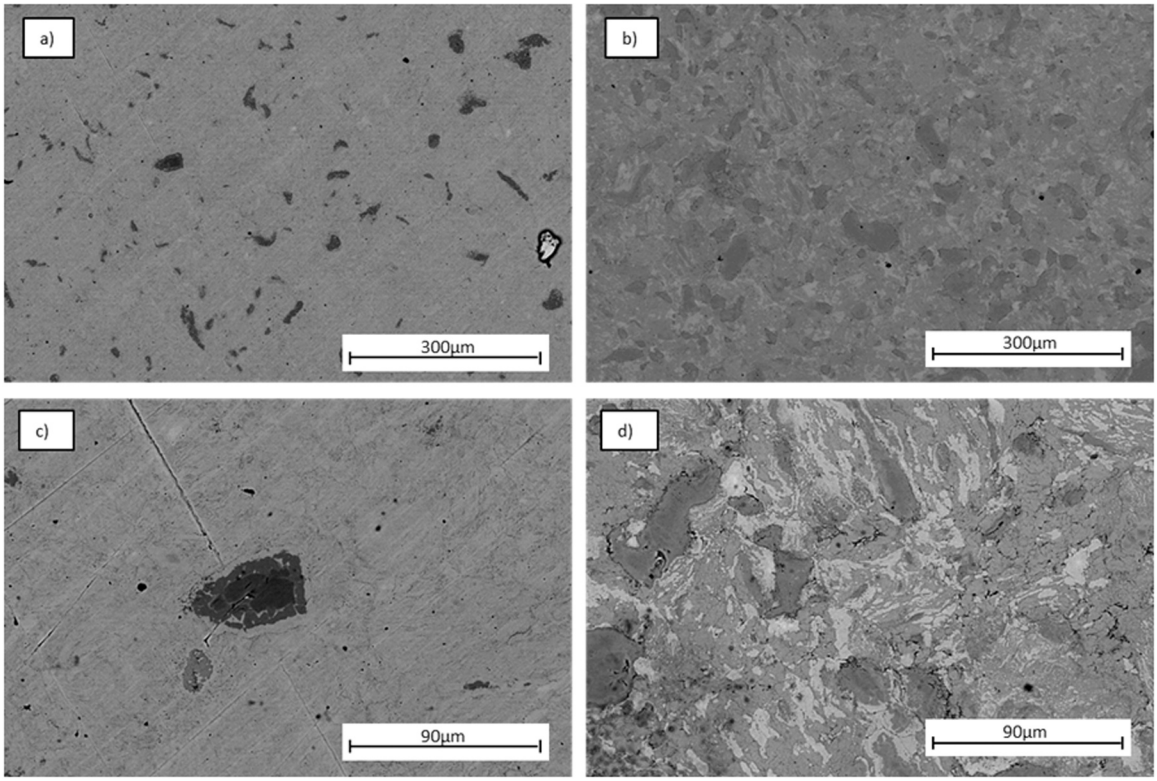

Fig. 1. Different magnifications SEM images of the surface for M1 **(a,c)** and M2 **(b,d)**.

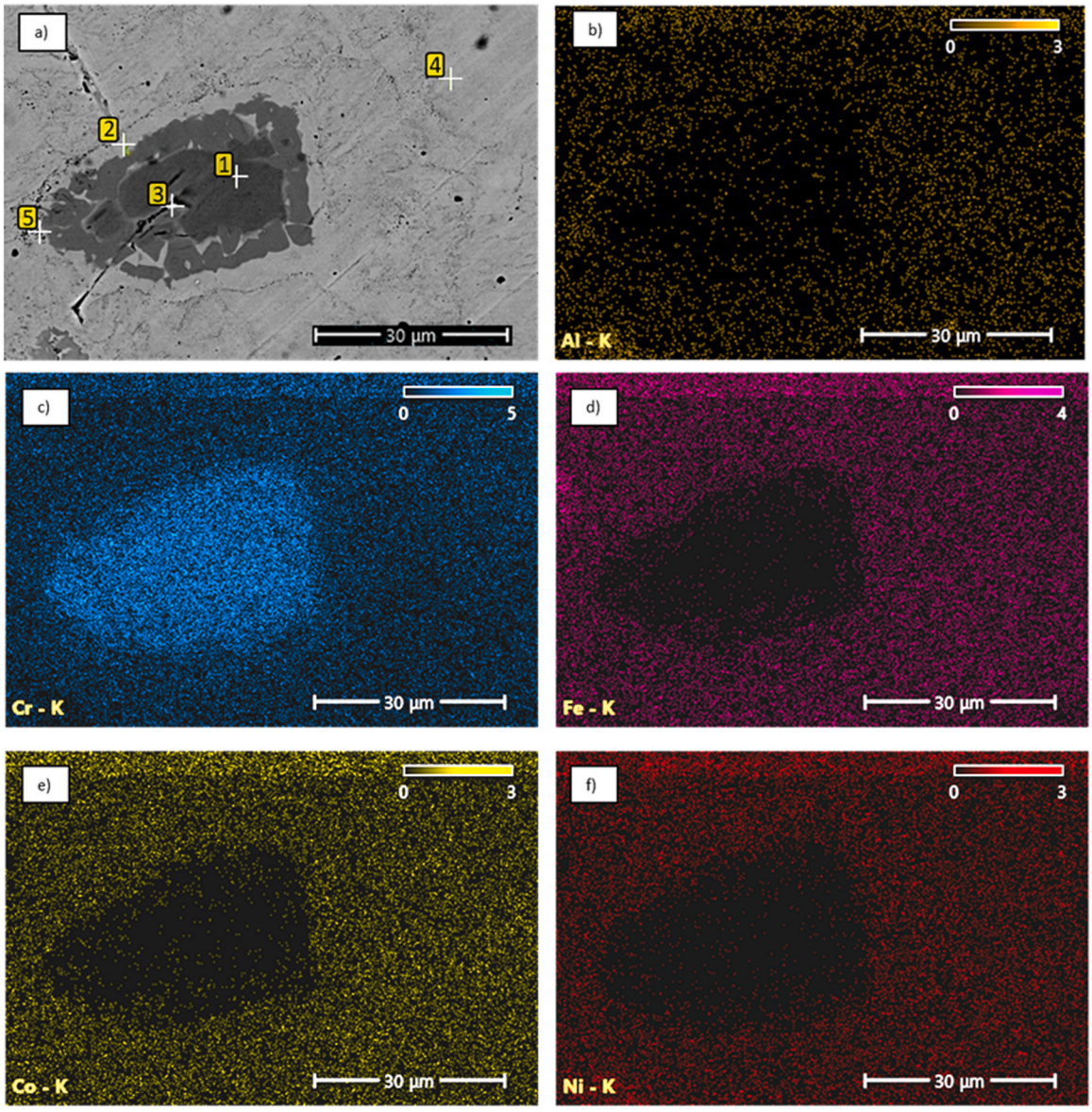

Fig. 2. Analysis points identification **(a)** and EDS mapping technique with color filter on M1 sample: **b)** Aluminum; **c)** Chromium; **d)** Iron; **e)** Cobalt; **f)** Nickel.

and carbon reach their relatively highest values, suggesting that boron carbide may have agglomerated in some areas.

Looking at the EDS mapping provided for sample M2 in Fig. 3, it can be seen that there is greater elemental segregation in the structure compared to sample M1. It can be interpreted that boron and carbon, which can be determined, are homogeneously distributed in the structure.

Analysis of the elemental maps revealed, as in M1, that chromium is concentrated in certain specific regions, where the distribution of aluminum is very limited. In contrast, iron, nickel and carbon are elements that are distributed more homogeneously within the structure.

In the study conducted by Mohsen Kivy and his collaborators [19], it was reported that, due to the free diffusion of carbon from the graphite crucible, chromium separates from the matrix and the $(Cr,Fe)_{23}C_6$ phase is formed.

The XRD patterns of samples M1 and M2 are shown in Fig. 4. In both samples, the peaks obtained were consistent with the (111), (200), and (220) planes and were similar to the standard diffraction pattern of FCC Ni (JCPDS: 00–004–0850) [47]. Both structures indicate the presence of a BCC phase, while the M1 sample is seen to have a predominantly FCC structure. This observation supports previous reports indicating that the addition of Al to the CoCrFeNi system promotes the coexistence of FCC and BCC phases and may lead to local chemical partitioning or element-rich regions rather than a single homogeneous phase, as discussed in detail in recent studies [48–50]. In addition to the FCC and BCC phases in the M1 sample, the σ (sigma) phase (JCPDS: 00–005–0708), represented by low-intensity peaks in the $2\theta \approx 35–45^\circ$ range, was detected [51]. The sigma phase is a brittle intermetallic compound that can form particularly in Cr-rich regions and may appear during the mechanical alloying process. After the SPS process, the σ phase did not completely disappear, although its diffraction intensity remained low, suggesting a limited volume fraction.

The addition of B_4C to the structure resulted in a more complex phase composition in sample M2. Additionally, peaks compatible with the BCC NiAl (JCPDS: 00–002–1261) phase were observed in the (110), (211), (200), and (100) planes [52]. Furthermore, the $M_{23}C_6$ carbide phase (JCPDS: 01–085–1281), characterized by multiple peaks in the $2\theta \approx 38–42^\circ$, $60–75^\circ$ range, is clearly evident. The formation of such carbide phases has been widely reported in carbon-containing or carbide-reinforced high-entropy alloys processed at elevated temperatures, where enhanced carbon diffusion during SPS promotes carbide precipitation, in good agreement with recent literature [53]. When

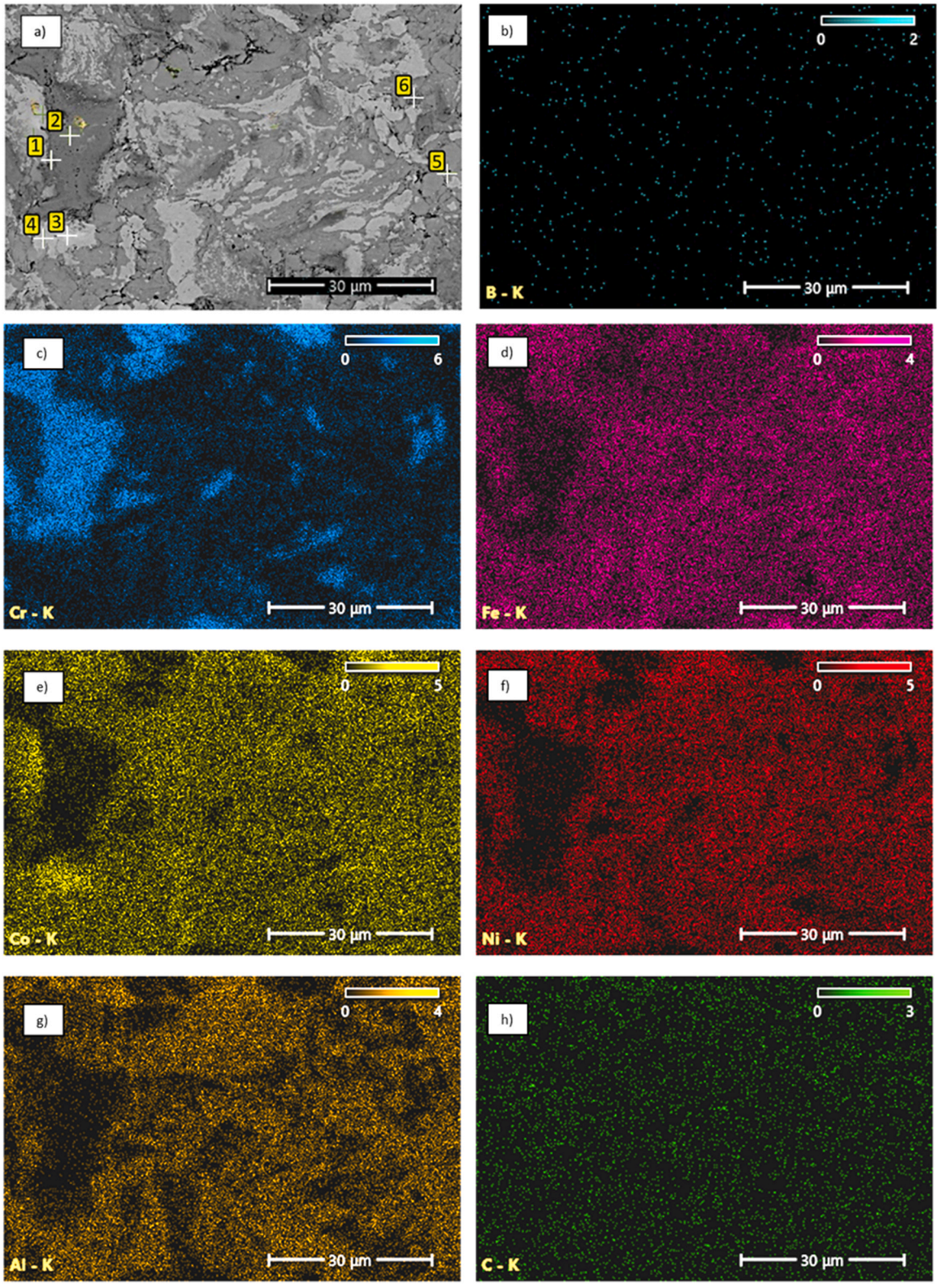

Fig. 3. Analysis points identification and EDS mapping technique with color filter under 5000x on M2 sample: a) Point identification; b) Boron; c) Chromium; d) Iron; e) Cobalt; f) Nickel; g) Aluminum; h) Carbon.

comparing the peak intensities and phases of both samples, it is observed that M2 exhibits a more complex and multi-phase structure due to its carbon content, while M1 has a relatively simple FCC + BCC + low amount of σ phase combination. The formation of the $M_{23}C_6$ phase in M2 indicates that carbide reactions occurred during SPS and that stable carbide phases were formed.

Below, Fig. 5 presents the metallographic observations obtained by optical microscopy. In sample M1, two distinct phases can be clearly distinguished, consistent with the features previously identified in the SEM analysis (Fig. 1). A slight surface porosity is also visible. In contrast,

Table 2
Atomic percentage on the different points selected at M1 sample.

	Atomic %				
Element	**P1**	**P2**	**P3**	**P4**	**P5**
Al	0.4	1.7	2.6	3.6	8.2
Cr	99.0	56.2	74.4	28.8	38.6
Fe	0.3	19.0	7.2	22.7	18.5
Co	0.1	14.2	7.6	22.1	17.9
Ni	0.3	8.9	8.2	22.9	16.8

Table 3
Atomic percentage on the different points selected at M2 sample.

	Atomic %					
Element	**P1**	**P2**	**P3**	**P4**	**P5**	**P6**
B	1.4	1.8	1.4	2.2	2.8	3.0
C	12.5	14.7	12.6	13.7	18.4	19.7
Al	11.2	1.0	5.3	7.8	23.1	11.2
Cr	48.6	69.3	7.4	10.5	2.5	23.6
Fe	10.1	6.5	7.7	24.8	14.7	18.5
Co	7.2	4.3	61.9	29.4	17.5	13.9
Ni	8.9	2.6	3.8	11.6	21.0	10.2

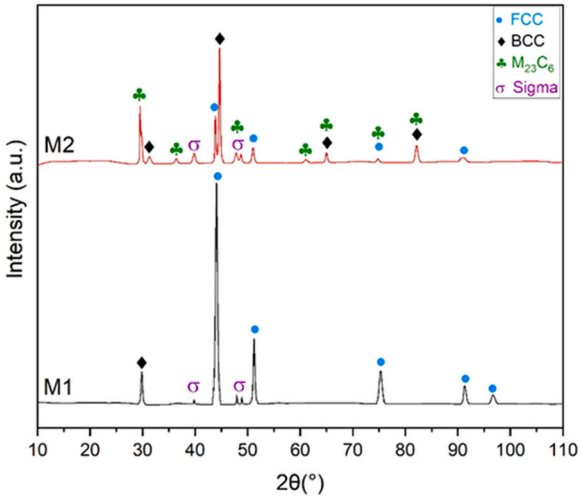

Fig. 4. XRD patterns of M1 and M2 samples.

the microstructure of M2 reveals a significantly more heterogeneous appearance, with a large number of dark inclusions distributed across the surface, corresponding to the presence of B_4C introduced during doping.

The segregation factor is a useful parameter to quantify how strongly an element accumulates in specific regions of a microstructure. A higher segregation ratio (SR) indicates that the element is concentrated in the most enriched area, meaning that the alloy exhibits a stronger degree of segregation.

In this work, the SR values, seen in Table 4, were calculated from SEM-EDS measurements by comparing the maximum and minimum local concentrations of each element. On both samples, the microstructure shows two clearly distinguishable contrast regions: a light-gray matrix (LG) and dark gray zones (DG) enriched in chromium. These two areas allow a direct comparison between the Cr-rich domains and the surrounding matrix.

$$SR = \frac{Element\ concentration\ in\ DG}{Element\ concentration\ in\ LG} \quad (1)$$

The SR values show clear chemical partitioning in both alloys. M1 exhibits strong segregation, especially for Cr in the darker regions. In M2, the segregation of Cr is stronger, with more than double SR factor. B_4C in M2 sample had a moderate segregation. Overall, the SR trends highlight that boron carbide doping increases the compositional contrast of the base HEA.

3.2. Electrochemical tests

3.2.1. Open circuit potential

Fig. 6 shows how the corrosion potential, E_{corr}, of both samples evolves during 24 h of immersion in 3.5 % NaCl solution. In the case of this kind of open-circuit potential (OCP) test, higher positive values are correlated with an improved degree of stability of the passive film and, consequently, a reduced tendency to corrode.

It can be observed that for sample M1, its potential is initially around –0.33 V vs SCE and in the first few hours it becomes slightly more negative, stabilizing at around –0.45 V. This behavior indicates that M1 quickly reaches a quasi-steady state and remains stable for the rest of the measurement, suggesting good corrosion resistance.

Sample M2 starts at a potential similar to that of M1 but within a few minutes quickly shifts to much more negative values (approx. −0.95 V vs SCE). During the measurement, it shows significant fluctuations without reaching a completely stable state.

3.2.2. Linear polarization

From the linear polarization curve (Fig. 7), it can be observed for sample M1 that the corrosion potential around −0.45 V vs. SCE coincides with the open circuit potential in Fig. 4. The passive region of M1 suggests the formation of a passive layer with stable products that limit

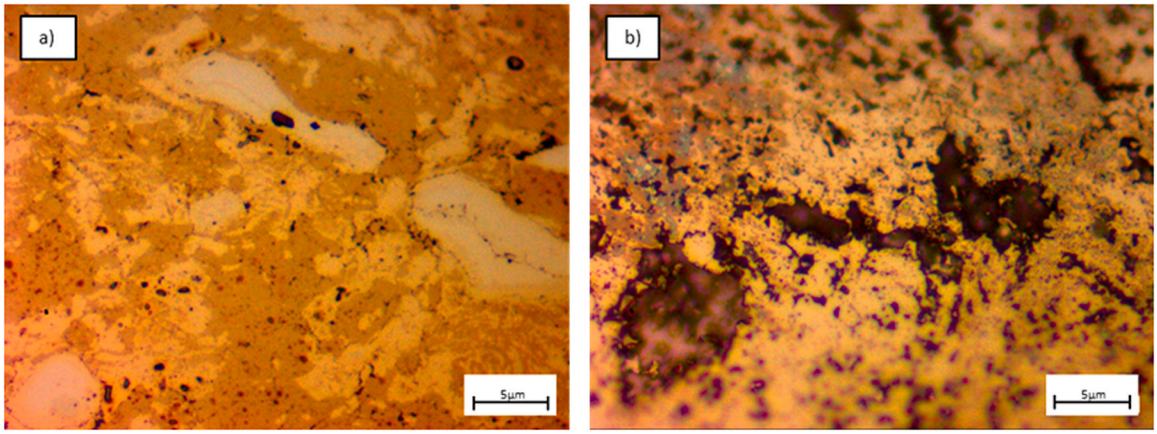

Fig. 5. Metallographic microscopy for: a) M1; b) M2.

Table 4
Composition average results in LG and DG areas and SR values of both samples.

Sample	Parameters	Al	Co	Cr	Fe	Ni	B	C
	LG	3.6	22.1	28.8	22.7	22.9	-	-
M1	DG	0.4	0.1	99.0	0.3	0.3	-	-
	SR	0.111	0.005	3.44	0.013	0.013	-	-
	LG	5.3	61.9	7.4	7.7	3.8	1.4	12.6
M2	DG	1.0	4.3	69.3	6.5	2.6	1.8	14.7
	SR	0.189	0.069	9.365	0.844	0.684	1.286	1.167

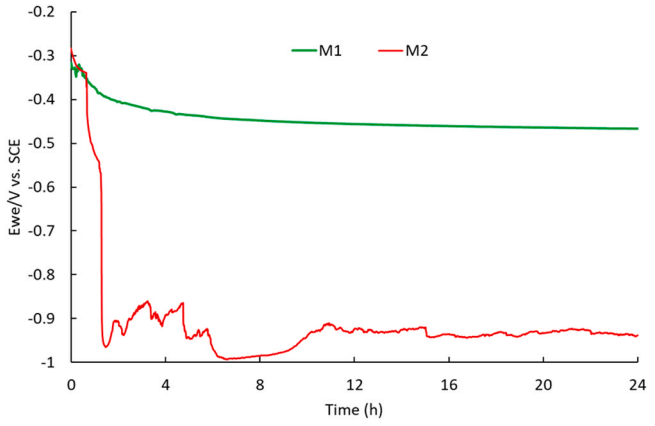

Fig. 6. OCP plot for 24 h immersion comparison for both samples in artificial sea water.

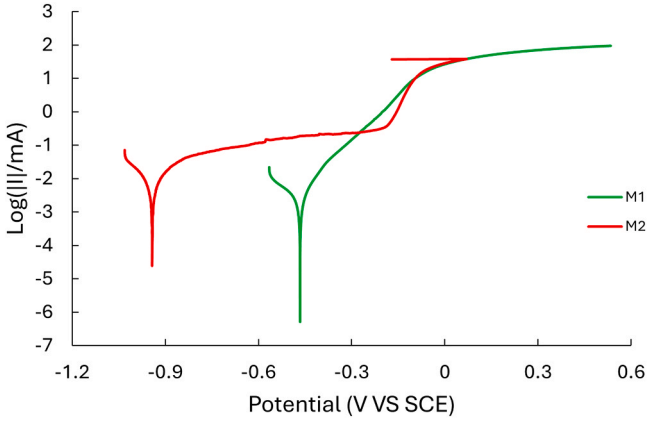

Fig. 7. Linear polarization curve comparison for both samples in artificial sea water.

the anodic reaction. The order of magnitude of the corrosion current is low (10^{-6}…10^{-7} A), indicating very good corrosion resistance. For sample M2, the corrosion potential is approximately −0.95 V, much more negative than that of M1. The corrosion current is much higher (10^{-4}…10^{-5} A) and the shape of the curve, together with the unstable OCP in Fig. 5, confirm pitting corrosion.

Table 5 shows the kinetic parameters of the corrosion process. The higher Tafel slopes for sample M2 indicate a breakdown of the passive film and instability of passivation, while M1 shows more moderate values, consistent with more stable passivation. M1 behaves as a material with more effective passivation and lower corrosion rate, while M2 behaves as a more active sample susceptible to localized corrosion. M2 passive layer behavior is probably due to chromium-carbon bonds, impeding the formation of a CrO_2 protective layer, as seen in SEM where chromium separates from the matrix and the $(Cr,Fe)_{23}$ C_6 phase is formed.

Table 5
Corrosion parameters for all samples tested.

Parameters	M1	M2
E_{corr} (mV vs. Ref)	-465.995	-941.769
I_{corr} (μA/cm^2)	0.137	2.516
β_c (mV)	6.0	47.5
β_a (mV)	5.8	45.8
Equivalent weight (g/eq)	21.033	20.953
Measured density (g/cm^3)	6.87 ± 0.008	6.91 ± 0.02
Surface (cm^2)	0.933	0.991
Corrosion rate (mmpy)	$1.470{\cdot}10^{-3}$	$25.189{\cdot}10^{-3}$

3.2.3. *Electrochemical impedance spectroscopy (EIS)*

The Nyquist diagrams are shown in Fig. 8 show a much larger semicircular arc for M1 than for M2, indicating a significantly higher load transfer resistance R_{ct} for sample M1. A higher R_{ct} is associated with a lower corrosion rate, especially because there are no dominant diffusion effects.

It can be observed that at low frequencies (from 100 mHz to 100 Hz) sample M1 has a higher IZI than sample M2 (see Fig. 9), which indicates greater resistance to charge transfer and, implicitly, greater resistance to corrosion. At high frequencies, the differences in IZI are small, demonstrating that the resistance of the solution is similar for both samples.

Both samples show a single broad minimum in the phase vs. frequency curve (see Fig. 10), suggesting a two-step corrosion process, typical of a simple R(QR)(QR) equivalent circuit, i.e., kinetic charge control through the passive film (see Fig. 11). However, M1 has a deeper phase minimum (approx. −70°) and is shifted to lower frequencies, indicating a higher effective capacitance associated with the passive film and a slower charge transfer process. M2 has a less pronounced phase minimum (approx. −50°), suggesting behavior with less capacitive accumulation due to a thinner or more defective passive layer.

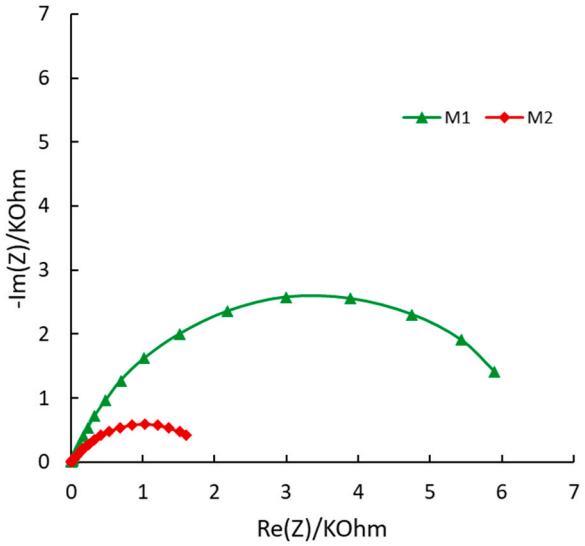

Fig. 8. Nyquist plot comparison for both samples in artificial sea water, with high frequencies magnification.

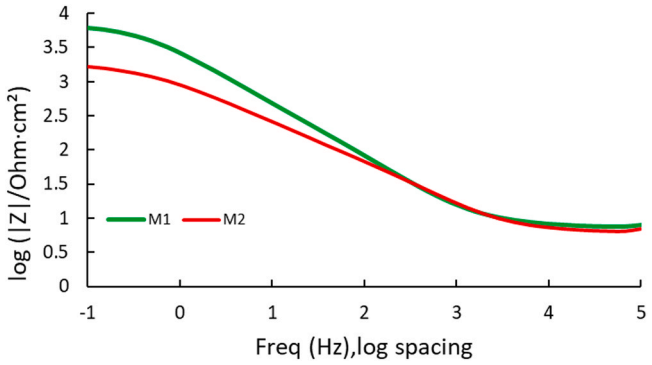

Fig. 9. Bode impedance comparison for both samples in artificial sea water.

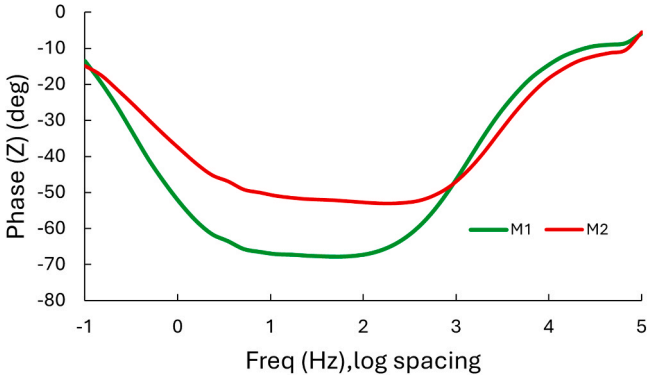

Fig. 10. Bode phase for both samples in artificial sea water.

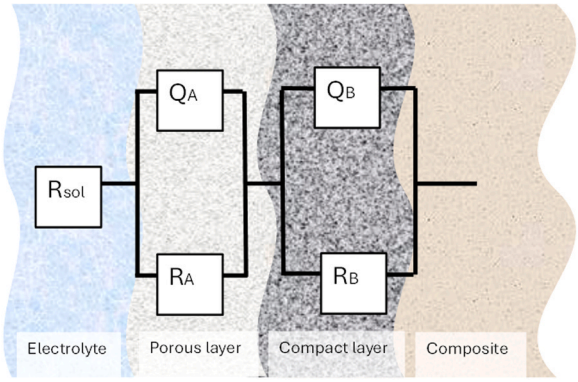

Fig. 11. R(QR)(QR) equivalent circuit for both composites in artificial sea water.

In Table 6, the equivalent circuit parameters are displayed. It can be seen that the parameters of the porous layer (R_A–Q_A) in both samples, present lower values than the ones found in their compact layer (R_B–Q_B), due to the effectiveness of the created inert protective fil on the samples surface. M1 values, in concordance with the other electrochemical tests conducted, present better corrosion behavior.

Table 6
R(QR)(QR) equivalent circuit parameters for composites under study.

Parameters	M1	M2
Y^0_A (S·sec^n/cm^2)	$7.16{\cdot}10^{-5}$	$2.27{\cdot}10^{-4}$
n_A	0.81	0.69
R_A (ohm·cm^2)	7.49	$2.33{\cdot}10^{1}$
Y^0_B (S·sec^n/cm^2)	$2.38{\cdot}10^{-8}$	$1.41{\cdot}10^{-4}$
n_B	1.00	0.90
R_B (ohm·cm^2)	$7.05{\cdot}10^{3}$	$1.95{\cdot}10^{3}$
Chi-square	$9.90{\cdot}10^{-4}$	$1.61{\cdot}10^{-3}$

In passive systems, "Q" denotes a Constant Phase Element (CPE). This circuit layout indicates that the surface has a two-layer passive film, with porous and compact regions that slow down dissolution before the electrolyte reaches the alloy. Applying Kirchhoff's laws and substituting the CPE terms leads to the following expression:

$$Z_{circuit} = R_{sol} + \frac{R_A \cdot Q_A}{R_A + Q_A} + \frac{R_B \cdot Q_B}{R_B + Q_B} \quad (2)$$

Where letters "*A*", "*B*", "*C*" and "*D*" stands for:

$$Q_A = \frac{1}{Y_A (jw)^{n_A}} \quad (3)$$

$$Q_B = \frac{1}{Y_B (jw)^{n_B}} \quad (4)$$

3.3. Vickers microhardness statistical analysis

The statistical analysis shows that M2 has a slightly higher average hardness than M1, as expected when adding a hard ceramic such as B_4C. However, according to the values in Table 7, M2 also presents a wider spread and higher standard deviation. This indicates that its hardness is less uniform across the sample. The boxplots and Gaussian curves confirm this trend, showing a broader distribution for M2, as seen in Fig. 12. This behavior is consistent with a more heterogeneous microstructure caused by the B_4C addition and its distribution after SPS sintering, according to SEM results. In contrast, M1 exhibits a narrower range of values, reflecting a more homogeneous alloy. Overall, the 2 % B_4C reinforcement increases hardness but also introduces greater variability.

4. Conclusion

This study investigated the effect of ceramic B_4C doping on the microstructural, mechanical and electrochemical behavior of equimolar AlCoCrFeNi HEA, processed by spark plasma sintering. Microstructural analysis revealed that the addition of B_4C leads to an increase in phase diversity on the homogeneous microstructure. Also, Cr-rich phases were observed in both M1 and M2 samples due to the mechanical alloying process and the high melting point of chromium. Ni and Al were observed to coexist with the most negative mixture enthalpy within the structure. XRD confirmed the existence of metallic carbides ($M_{23}C_6$) on the doped sample and in SEM it was observed that B and C elements concentrated in the Cr-rich region due to their mixture enthalpies.

The Vicker test results demonstrate that B_4C addition leads to a clear increase in hardness primarily attributed to the ceramic reinforcement, although at the expense of a less uniform distribution of mechanical response. However, this mechanical enhancement is accompanied by a greater degradation in corrosion resistance. The doped sample presented a higher susceptibility to corrosion, associated with a less effective protective film. This is mainly produced by the $M_{23}C_6$ phase formation.

Table 7
Statistical parameters of Vickers hardness measurements for both samples.

Statistical Parameters	Hardness ($HV_{0.1}$)	
	M1	M2
Mean	451	456
Median	447	452
Standard deviation	33	45
Minimum	368	392
Maximum	524	593
Quartile 25	428	421
Quartile 50	447	452
Quartile 75	474	481

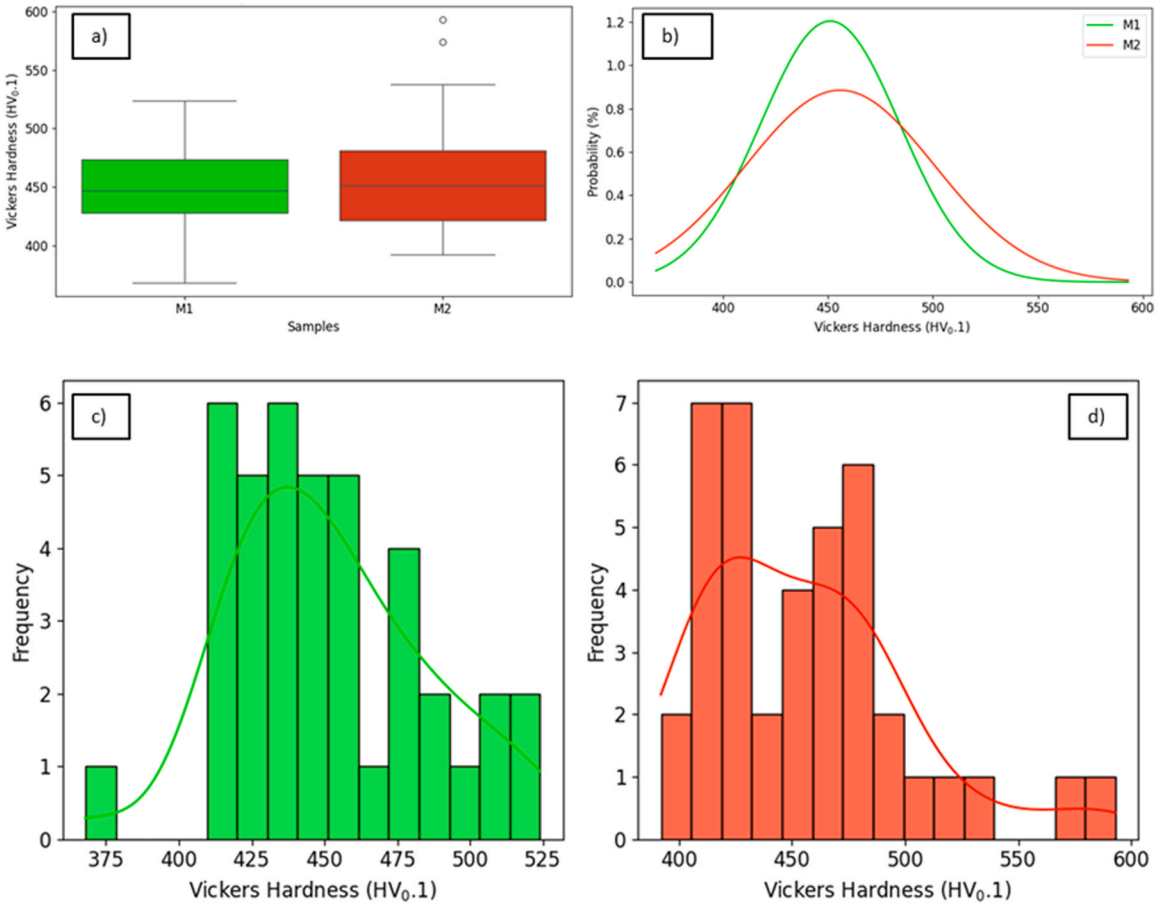

Fig. 12. Vickers hardness statistical analysis and comparison by: (a) data distribution through its quartiles; b) probability distribution; c) histogram for M1; d) histogram for M2.

Due to carbon free diffusion, chromium separates from the matrix and the $Cr_{23}C_6$ phase is formed, being enabled to form protective chromium oxides (Cr_2O_3) which prevent corrosion on the material surface.

From a practical perspective, M2 may be suitable for applications where high hardness and wear resistance are critical, but in controlled atmospheres. In extremely aggressive environments, such as biomedicine, energy storage or shipbuilding [54], the best option for corrosion resistance and long-term durability is M1.

Future work employing both materials should focus on B_4C doping optimization in order to balance mechanical and electrochemical properties. Also, post-sintering heat treatments are another aspect to consider. Finally, other carbides can be considered and studied to substitute B_4C, such as SiC or TiC, to try to improve AlCoCrFeNi HEA mechanical properties without compromising its corrosion behavior.

CRediT authorship contribution statement

Alberto Daniel Rico-Cano: Writing – review & editing, Writing – original draft, Methodology, Investigation, Formal analysis, Data curation, Conceptualization. **Göknur Karadeniz:** Writing – review & editing, Writing – original draft, Investigation, Formal analysis, Data curation. **Julia Claudia Mirza-Rosca:** Visualization, Validation, Supervision. **Gultekin Goller:** Visualization, Validation, Supervision, Conceptualization.

Declaration of Competing Interest

The authors declare that they have no known competing financial interests or personal relationships that could have appeared to influence the work reported in this paper.

References

[1] B. Cantor, I.T.H. Chang, P. Knight, A.J.B. Vincent, Microstructural development in equiatomic multicomponent alloys, Mater. Sci. Eng. A (2004) *375–377*, https://doi.org/10.1016/J.MSEA.2003.10.257.
[2] J.W. Yeh, Recent Progress in High-Entropy Alloys, Annales de Chimie Science des Materiaux 31 (2006) 633–648, https://doi.org/10.3166/acsm.31.633-648.
[3] D. Castro, P. Jaeger, A.C. Baptista, J.P. Oliveira, An overview of high-entropy alloys as biomaterials, Metals 11 (2021).
[4] G. Cui, B. Han, Y. Yang, Y. Wang, H. Chunyang, Microstructure and tribological property of CoCrFeMoNi high entropy alloy treated by ion sulfurization, J. Mater. Res. Technol. 9 (2020) 2598–2609, https://doi.org/10.1016/j.jmrt.2019.12.090.
[5] F. Yang, J. Wang, Y. Zhang, Z. Wu, Z. Zhang, F. Zhao, J. Huot, J. Grobivć Novaković, N. Novaković, Recent progress on the development of high entropy alloys (HEAs) for solid hydrogen storage: a review, Int. J. Hydrog. Energy 47 (2022) 11236–11249.
[6] H. Yang, Z. Shao, Q. Lu, C. Cui, L. Xu, G. Yang, Development of reduced-activation and radiation-resistant high-entropy alloys for fusion reactor, Int. J. Refract. Met. Hard Mater. 121 (2024) 106674, https://doi.org/10.1016/J.IJRMHM.2024.106674.
[7] Z.Q. Xu, Z.L. Ma, M. Wang, Y.W. Chen, Y.D. Tan, X.W. Cheng, Design of novel low-density refractory high entropy alloys for high-temperature applications, Mater. Sci. Eng. A 755 (2019) 318–322, https://doi.org/10.1016/J.MSEA.2019.03.054.
[8] P. Chakraborty, A. Sarkar, K. Ali, J. Jha, N. Jothilakshmi, A. Arya, R. Tewari, Design and development of low density, high strength ZrNbAlVTi high entropy alloy for high temperature applications, Int. J. Refract. Met. Hard Mater. 113 (2023) 106222, https://doi.org/10.1016/J.IJRMHM.2023.106222.
[9] Y. Kozhakhmetov, M. Skakov, S. Kurbanbekov, G. Uazyrkhanova, A. Kurmantayev, A. Kizatov, N. Mussakhan, High-entropy alloys: innovative materials with unique properties for hydrogen storage and technologies for their production, Metals 15 (2025).
[10] Y. Zhou, K. Chen, Y. You, X. Shang, Y. Li, H. Shi, J. Dang, K. Zhang, S. Lozano-Perez, L. Zhang, et al., Oxide stress and fracture susceptibility on a surface gradient microstructure of an additively manufactured Steel, Acta Mater. 304 (2026) 121779, https://doi.org/10.1016/J.ACTAMAT.2025.121779.

[11] Y. Zhou, H. Hu, C. Peng, J. Liu, Y. Zhao, X. Shang, C. Guo, Z. Shen, M. Song, L. Zhang, et al., A precipitation hardened austenitic stainless steel with excellent stress corrosion cracking resistance against high-temperature water, Corros. Sci. 257 (2025) 113352, https://doi.org/10.1016/J.CORSCI.2025.113352.

[12] D. Luo, Q. Zhou, W. Ye, Y. Ren, C. Greiner, Y. He, H. Wang, Design and characterization of self-lubricating refractory high entropy alloy-based multilayered films, ACS Appl. Mater. Interfaces 13 (2021) 55712–55725, https://doi.org/10.1021/acsami.1c16949.

[13] Y. Ma, Z. Jiao, Z. Huang, Q. Zhou, T. Huang, X. Ran, Z. Wang, L. Qiu, H. Teng, X. Lu, et al., Exploration on the oxidation resistance of TiAlNbN films: mechanisms of nanopore regulation and crack suppression, Corros. Sci. 257 (2025) 113273, https://doi.org/10.1016/J.CORSCI.2025.113273.

[14] M.L. Rios, V.L. Baldevenites, I. Voiculescu, J.M. Rosca, AlCoCrFeNi high entropy alloys as possible nuclear materials, Microsc. Microanal. 26 (2020) 406–407, https://doi.org/10.1017/s1431927620014555.

[15] M. Tokarewicz, M. Grądzka-Dahlke, Review of recent research on alcocrfeni high-entropy alloy, Metals 11 (2021).

[16] N. Florido-Suarez, P. Socorro-Perdomo, V. Geanta, J. Mirza-Rosca, Effect of heat treatment on the microstructure and corrosión resistance of AlCoCrFeNi high-entropy alloy, Microsc. Microanal. 27 (2021) 3372–3374, https://doi.org/10.1017/s1431927621011594.

[17] P.F. Zhou, D.H. Xiao, T.C. Yuan, Microstructure, mechanical and corrosion properties of AlCoCrFeNi high-entropy alloy prepared by spark plasma sintering, Acta Metall. Sin. (Engl. Lett.) 33 (2020) 937–946, https://doi.org/10.1007/s40195-019-00962-8.

[18] P.P. Socorro-Perdomo, N.R. Florido-Suárez, I. Voiculescu, J.C. Mirza-Rosca, Comparative Eis study of alxcocrfeni alloys in ringer's solution for medical instruments, Metals 11 (2021), https://doi.org/10.3390/met11060928.

[19] M. Beyramali Kivy, C.S. Kriewall, M. Asle Zaeem, Formation of chromium-iron carbide by carbon diffusion in AlXCoCrFeNiCu high-entropy alloys, Mater. Res. Lett. 6 (2018) 321–326, https://doi.org/10.1080/21663831.2018.1449767.

[20] K. Xiong, L. Huang, X. Wang, L. Yu, W. Feng, Microstructure, mechanical properties, and damping capacity of AlxCoCrFeNi high-entropy alloys prepared by spark plasma sintering, Metals 12 (2022), https://doi.org/10.3390/met12122058.

[21] A.D. Rico-Cano, J.C. Mirza-Rosca, B.C. Ocak, G. Goller, Impact of CoCrFeNiMo high-entropy-alloy doping on the mechanical and electrochemical properties of B4C ceramic, Appl. Sci. 15 (2025), https://doi.org/10.3390/app15094859.

[22] S.J. Brito-Garcia, J.C. Mirza-Rosca, C. Jimenez-Marcos, I. Voiculescu, Impact of Ti doping on the microstructure and mechanical properties of CoCrFeMoNi high-entropy alloy, Metals 13 (2023), https://doi.org/10.3390/met13050854.

[23] X. Wen, X. Zhang, L. Song, Y. Gong, F. Han, Strengthening mechanism of laser cladding FeCoNiCrAl high-entropy alloy with different contents of SiC ceramic particles, Ceram. Int. 51 (2025) 29599–29609, https://doi.org/10.1016/J.CERAMINT.2025.04.163.

[24] Ł. Rogal, D. Kalita, A. Tarasek, P. Bobrowski, F. Czerwinski, Effect of SiC nano-particles on microstructure and mechanical properties of the CoCrFeMnNi high entropy alloy, J. Alloy. Compd. 708 (2017) 344–352, https://doi.org/10.1016/J.JALLCOM.2017.02.274.

[25] X. Han, E. Liu, C. Peng, C. Han, G. Zhou, C. Li, L. Qi, R. Li, Y. Ke, Synthesis and characterization of TiB2-reinforced AlCoCrFeNi2.1 high-entropy-alloy matrix composite, Metals) 14 (2024), https://doi.org/10.3390/met14121325.

[26] J. Huang, F. Luo, Y. Zhao, W. Shi, Preparation of AlCoCrFeNi/W-TiC HEA composite coating by laser cladding, Mater. Today Commun. 39 (2024) 108677, https://doi.org/10.1016/J.MTCOMM.2024.108677.

[27] D. Liu, D. Kong, Effects of WC–10Co4Cr and TiC additions on microstructure and tribological properties of laser cladded FeMnCoCr HEA coatings, Ceram. Int. 50 (2024) 12108–12120, https://doi.org/10.1016/J.CERAMINT.2024.01.115.

[28] A.O. Gul, E. Kavaz, O. Basgoz, O. Guler, G. ALMisned, E. Bahceci, M.G. Albayrak, H.O. Tekin, Newly synthesized NiCoFeCrW high-entropy alloys (HEAs): multiple impacts of B4C additive on structural, mechanical, and nuclear shielding properties, Intermetallics 146 (2022) 107593, https://doi.org/10.1016/J.INTERMET.2022.107593.

[29] S.Y. Ahn, F. Haftlang, E.S. Kim, S.G. Jeong, J.S. Lee, H.S. Kim, Boost in mechanical strength of additive manufactured CoCrFeMnNi HEA by reinforcement inclusion of B4C nano-particles, J. Alloy. Compd. 960 (2023) 170631, https://doi.org/10.1016/J.JALLCOM.2023.170631.

[30] A.D. Rico-Cano, J.C. Mirza-Rosca, B.C. Ocak, G. Goller, Corrosion behavior and microhardness of a new B4C ceramic doped with 3% volume high-entropy alloy in an aggressive environment, Metals 15 (2025) 79, https://doi.org/10.3390/met15010079.

[31] B. Yavas, F. Sahin, O. Yucel, G. Goller, Effect of particle size, heating rate and CNT addition on densification, microstructure and mechanical properties of B4C ceramics, Ceram. Int. 41 (2015) 8936–8944, https://doi.org/10.1016/j.ceramint.2015.03.167.

[32] S. Pérez, P. Tamayo, J. Rico, J. Alonso, C. Thomas, Effect of fibers and boron carbide on the radiation shielding properties of limestone and magnetite aggregate concrete, Prog. Nucl. Energy 175 (2024), https://doi.org/10.1016/j.pnucene.2024.105320.

[33] A.K. Suri, C. Subramanian, J.K. Sonber, T.S.R. Ch Murthy, Synthesis and consolidation of boron carbide: a review, Int. Mater. Rev. 55 (2010) 4–38.

[34] V. Domnich, S. Reynaud, R.A. Haber, M. Chhowalla, Boron carbide: structure, properties, and stability under stress, J. Am. Ceram. Soc. 94 (2011) 3605–3628, https://doi.org/10.1111/j.1551-2916.2011.04865.x.

[35] W. Zhang, A review of tribological properties for boron carbide ceramics, Prog. Mater. Sci. 116 (2021).

[36] B.M. Moshtaghioun, F.L. Cumbrera-Hernández, D. Gómez-García, S. de Bernardi-Martín, A. Domínguez-Rodríguez, A. Monshi, M.H. Abbasi, Effect of spark plasma sintering parameters on microstructure and room-temperature hardness and toughness of fine-grained boron carbide (B4C), J. Eur. Ceram. Soc. 33 (2013) 361–369, https://doi.org/10.1016/J.JEURCERAMSOC.2012.08.028.

[37] E.M. Pirot, A.N. Faqi, R.F. Jader, M.M. Mamash, I.H. Jumaa, R.M. Hussein, D. M. Sharif, Comparative study of the pore volume percentages of the carbonate core plug samples using direct, 2D techniques and exploratory data analysis, Flow. Meas. Instrum. 102 (2025) 102813, https://doi.org/10.1016/J.FLOWMEASINST.2025.102813.

[38] T.J. Collins, ImageJ for microscopy, Biotechniques 43 (2007), https://doi.org/10.2144/000112517.

[39] T. Thilagashanthi, K. Gunasekaran, K.S. Satyanarayanan, Microstructural pore analysis using SEM and imagej on the absorption of treated coconut shell aggregate, J. Clean. Prod. 324 (2021) 129217, https://doi.org/10.1016/J.JCLEPRO.2021.129217.

[40] C. Material, P. Databases, Standard reference test method for making potentiostatic and potentiodynamic anodic, Annu. B ASTM Stand 94 (2004) 1–12.

[41] ISO 16773-1-4:2016 Electrochemical Impedance Spectroscopy (EIS) on Coated and Uncoated Metallic Specimens n.d. ISO: Geneva, Switzerland 2016.

[42] ISO 14577-1:2015 Metallic Materials—Instrumented Indentation Test for Hardness and Materials Parameters—Part 1: Test Method n.d. ISO: Geneva, Switzerland 2015.

[43] G. Li, X. Meng, C. Geng, C. Wang, H. Ren, X. Guo, S. Li, Y. Tao, Microstructure and properties of AlxCr1−xCoFeNi high-entropy alloys prepared by spark plasma sintering, Materials 18 (2025), https://doi.org/10.3390/ma18040755.

[44] O.T. Onawale, P.V. Cobbinah, R.A. Nzeukou, W.R. Matizamhuka, Synthesis route, microstructural evolution, and mechanical property relationship of high-entropy alloys (HEAs): a review, Materials 14 (2021).

[45] Z. Wu, M. He, H. Cao, S. Wang, R. Chen, B. Cao, R. Shi, X. Liu, S. Yu, S. Wang, et al., Ultrahigh-strength and ductile CoCrFeNi-based high-entropy alloys manufactured by laser powder bed fusion with multiple strengthening mechanisms, J. Mater. Res. Technol. 25 (2023) 2948–2960, https://doi.org/10.1016/j.jmrt.2023.06.110.

[46] W. Chen, Z. Fu, S. Fang, H. Xiao, D. Zhu, Alloying behavior, microstructure and mechanical properties in a FeNiCrCo0.3Al0.7 high entropy alloy, Mater. Des. 51 (2013) 854–860, https://doi.org/10.1016/j.matdes.2013.04.061.

[47] G. Li, X. Meng, C. Geng, C. Wang, H. Ren, X. Guo, S. Li, Y. Tao, Microstructure and properties of AlxCr1−xCoFeNi high-entropy alloys prepared by spark plasma sintering, Materials 18 (2025), https://doi.org/10.3390/ma18040755.

[48] S. Arun, N. Radhika, B. Saleh, Effect of additional alloying elements on microstructure and properties of AlCoCrFeNi high entropy alloy system: a comprehensive review, Met. Mater. Int. 31 (2025) 285–324, https://doi.org/10.1007/s12540-024-01752-3.

[49] R. Jiang, E. Torresani, A. Maximenko, H. Wang, S. Faulhaber, K. Vecchio, E. A. Olevsky, Cyclic phase transition-assisted spark plasma sintering of AlCoCrFeNi complex concentrated alloys, Metall. Mater. Trans. A Phys. Metall. Mater. Sci. 55 (2024) 1111–1121, https://doi.org/10.1007/s11661-024-07308-9.

[50] Q. Zhou, Z. Jiao, Z. Huang, Y. Shi, Y. Li, C. Yin, H. Wang, H.C. Pinto, C. Greiner, W. Liu, Wear-resistant CrCoNi NAnocrystalline Film Via Friction-driven Surface Segregation, Acta Mater. 279 (2024) 120299, https://doi.org/10.1016/J.ACTAMAT.2024.120299.

[51] E.G. Campari, A. Casagrande, Microstructural study of CrNiCoFeMn high entropy alloy obtained by selective laser melting, Materials 15 (2022), https://doi.org/10.3390/ma15165544.

[52] M.H. Enayati, F. Karimzadeh, S.Z. Anvari, Synthesis of nanocrystalline NiAl by mechanical alloying, J. Mater. Process. Technol. 200 (2008) 312–315, https://doi.org/10.1016/J.JMATPROTEC.2007.09.023.

[53] W. Ye, M. Xie, Q. Zhou, B. Chen, Y. Li, L. Jia, H. Wang, W. Liu, Superior wear performance of CoCrNi matrix composite reinforced with quasi-continuously networked graphene nanosheets and in-situ carbide, Friction 13 (2025), https://doi.org/10.26599/FRICT.2025.9441001.

[54] V.E. Gromov, Y.A. Shlyarova, S.V. Konovalov, S.V. Vorob'ev, O.A. Peregudov, Application of high-entropy alloys, Steel Transl. 51 (2021) 700–704, https://doi.org/10.3103/S096709122110003X.